Computers in Biology and Medicine 136 (2021) 104661

Contents lists available at ScienceDirect

Computers in Biology and Medicine

journal homepage: www.elsevier.com/locate/compbiomed

A clinical-in silico study on the effectiveness of multipoint bicathodic and cathodic-anodal pacing in cardiac resynchronization therapy

G. Dell'Era [a], M. Gravellone [b], S. Scacchi [c,*], P. Colli Franzone [d], L.F. Pavarino [d], E. Boggio [b], E. Prenna [a], F. De Vecchi [e], E. Occhetta [e], C. Devecchi [e], G. Patti [a,f]

[a] Cardiologia 1, Azienda Ospedaliera Universitaria "Maggiore Della Carità", Novara, Italy
[b] Divisione di Cardiologia, Ospedale Degli Infermi, Biella, Italy
[c] Dipartimento di Matematica, Università Degli Studi di Milano, Via Saldini 50, 20133, Milano, Italy
[d] Dipartimento di Matematica, Università Degli Studi di Pavia, Via Ferrata 1, 27100, Pavia, Italy
[e] Divisione di Cardiologia, Ospedale Sant'Andrea, Vercelli, Italy
[f] Dipartimento di Medicina Traslazionale, Università Del Piemonte Orientale, Novara, Italy

ARTICLE INFO

Keywords:
Cardiac resynchronization therapy
Multipoint pacing
Cathodic-anodal pacing
Cardiac electromechanical simulations
Bidomain model

ABSTRACT

Up to one-third of patients undergoing cardiac resynchronization therapy (CRT) are *nonresponders*. Multipoint bicathodic and cathodic-anodal left ventricle (LV) stimulations could overcome this clinical challenge, but their effectiveness remains controversial. Here we evaluate the performance of such stimulations through both *in vivo* and *in silico* experiments, the latter based on computer electromechanical modeling. Seven patients, all candidates for CRT, received a quadripolar LV lead. Four stimulations were tested: right ventricular (RVS); conventional single point biventricular (S-BS); multipoint biventricular bicathodic (CC-BS) and multipoint biventricular cathodic-anodal (CA-BS). The following parameters were processed: **QRS** duration; maximal time derivative of arterial pressure ($\mathbf{dPdt}_{max}$); systolic arterial pressure ($\mathbf{P}_{sys}$); and stroke volume (**SV**). Echocardiographic data of each patient were then obtained to create an LV geometric model. Numerical simulations were based on a strongly coupled Bidomain electromechanical coupling model.

Considering the *in vivo* parameters, when comparing S-BS to RVS, there was no significant decrease in **SV** (from 45 ± 11 to 44 ± 20 ml) and 6% and 4% increases of $\mathbf{dPdt}_{max}$ and $\mathbf{P}_{sys}$, respectively. Focusing on *in silico* parameters, with respect to RVS, S-BS exhibited a significant increase of **SV**, $\mathbf{dPdt}_{max}$ and $\mathbf{P}_{sys}$. Neither the *in vivo* nor *in silico* results showed any significant hemodynamic and electrical difference among S-BS, CC-BS and CA-BS configurations.

These results show that CC-BS and CA-BS yield a comparable CRT performance, but they do not always yield improvement in terms of hemodynamic parameters with respect to S-BS. The computational results confirmed the *in vivo* observations, thus providing theoretical support to the clinical experiments.

1. Introduction

Cardiac resynchronization therapy (CRT) is an established treatment for heart failure. CRT has been proven beneficial in improving symptoms, inducing reverse remodeling, and reducing hospitalizations and mortality in patients with heart failure with reduced ejection fraction (HFrEF) [7,30,39]. However, in about 30% of patients who fulfill indications for CRT symptoms, ejection fraction (EF), and prognosis do not improve [1]. These *nonresponders* patients remain a clinical challenge.

In this regard, several solutions have been proposed, ranging from better selection of candidates to echocardiographic optimization of atrioventricular and ventriculo-ventricular delay. Technical evolution has currently produced quadripolar lead, opening new perspectives in CRT. Multipoint pacing (MPP), delivering two different left ventricular pacing vectors chosen among the different possible configurations by a quadripolar lead in a single coronary sinus branch, could enable more ventricular tissue capture for better intraventricular conduction [5]. A few previous studies have shown that MPP acutely improves contractility, hemodynamics, and dyssynchrony [34,42,56], whereas long-term clinical results remain controversial [9,35]. Results from the phase-1 MORE-CRT MPP [28] study have shown that MPP programming does not significantly increase echocardiographic response compared to

* Corresponding author.
E-mail address: simone.scacchi@unimi.it (S. Scacchi).

https://doi.org/10.1016/j.compbiomed.2021.104661
Received 7 April 2021; Received in revised form 16 July 2021; Accepted 16 July 2021
Available online 22 July 2021

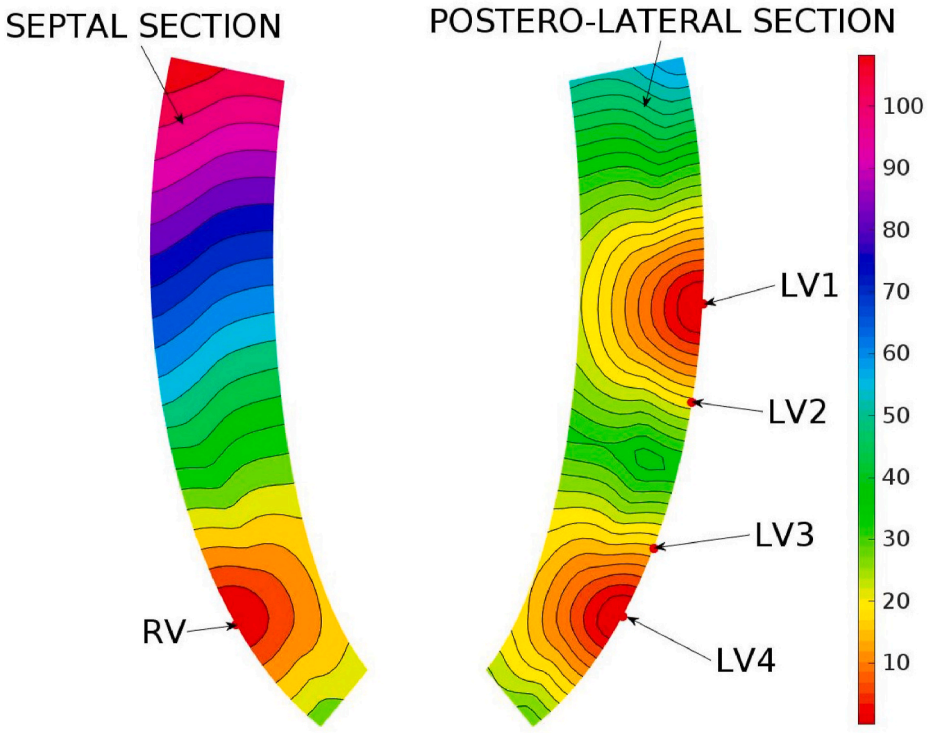

Fig. 1. Schematic representation of stimulating electrode positions. In the RVS stimulation, the stimulus is applied at the RV lead; in the S-BS stimulation, the stimulus is applied at the RV and LV1 leads; in the CC-BS and CA-BS stimulations, the stimulus is applied at the RV, LV1 and one among LV2, LV3, or LV4 leads, depending on the patient. In RVS, S-BS, and CC-BS stimulations, all pacing leads are cathodes. In the CA-BS stimulation, one of the LV leads is an anode. The colors refer to the activation time isochrones computed from the CC-BS stimulation in patient 4, with the step amounting to 5 ms.

conventional biventricular pacing.

Computer electromechanical modeling is a promising effective tool to support *in vivo* investigations, with the possibility to explore multiple pacing parameters [2,14,15,25,31,49,53]. However, most of these previous studies have focused on conventional single point biventricular stimulation. To our knowledge a detailed comparison between *in vivo* and *in silico* data on several patient models and considering different hemodynamic and electrical parameters is still lacking in the literature.

Anodal capture is a type of cardiac stimulation achieved by hyperpolarizing myocardial cells at the lead interface and depolarizing virtual electrode sites at some distance from the lead tip (anode make phenomenon) or depolarizing the lead location once the anodal stimulus is terminated (anode break phenomenon) [10,11,41,47,48,55]. Until now, the usual anodal capture during CRT is the right ventricular (RV) anodal capture delivered by pseudo-bipolar configurations, where the RV ring is the anode. However, the resulting stimulation has been considered an undesirable side-effect [8,18,51]. On the other hand, a beneficial anodal left ventricular (LV) stimulation, simultaneous to the cathodic stimulation, can be obtained during CRT, using a bipolar or preferably quadripolar LV lead in which the proximal and distal electrodes serve as the cathode and the anode interfacing and depolarizing the myocardium. This so-called cathodic-anodal stimulation may activate a larger volume of LV myocardium than cathodal pacing of identical intensity by a nearly flat activation wavefront [20, Fig. 1]. In a previous paper, we demonstrated that additional anodal capture by the proximal LV ring during LV pacing was possible in most recipients of a resynchronization device equipped with a multipolar LV lead [33]. In our further study [17], we have shown that cathodic-anodal LV stimulation is feasible and that it produces an electrical equivalence to MPP in terms of similar QRS wavefront activation. To our knowledge, no prior study has reported a hemodynamic evaluation of cathodic-anodal LV stimulation.

The aims of the present study were: to explore both the acute hemodynamic and electrical effects of different CRT configurations (single point CRT, bicathodic CRT and cathodic-anodal CRT) in patients with HFrEF (two of them with scar due to myocardial infarction); and to compare these data with hemodynamic and electrical parameters computed from the numerical simulations of the LV models, based on the cardiac electromechanical coupling model. In the numerical simulations reported, we use a cardiac electromechanical coupling model consisting of the so-called Bidomain model [37] and a finite elasticity model [13,14,24,40,53] for the electrophysiological and mechanical descriptions of the myocardial tissue, respectively. In the construction of the model, we consider the same calibration of the bioelectrical and

Table 1
Clinical characteristics of patients.

Number of patients	7
Sex (M/F)	M: 5 (72%)
	F: 2 (28%)
Mean age (*years*)	67.8 ± 11.55
BMI (Kg/m^2)	25.4 ± 6.1
NYHA functional class	I: 0
	II: 4 (57%)
	III: 3 (43%)
	IV: 0
Cardiomyopathy	Ischemic: 2 (28%)
	Post-myocarditis: 1 (14%)
	Valvular: 2 (28%)
	Idiopathic: 2 (28%)
Basal rhythm	Sinus rhythm: 6 (86%)
	Atrial fibrillation: 1 (14%)
Spontaneous QRS duration (*ms*)	142 ± 27
LV EF (%)	31.4 ± 8.6
Telediastolic volume (*ml*)	132.7 ± 69.2
Telesystolic volume (*ml*)	94.5 ± 59.5
CRT device	ICD: 3 (43%)
	PM: 4 (57%)
Target vein (Left anterior oblique projection)	Lateral: 3 (43%)
	Posterior: 4 (57%)
Target vein (Right anterior oblique projection)	Basal: 1 (14%)
	Mid: 6 (86%)
CC-BS, bicathodic dipole	LV1-LV4: 4 (57%)
	LV1-LV2: 2 (28%)
	LV1-LV3: 1 (15%)
CA-BS, cathodic-anodal bipole	LV1-LV4: 4 (57%)
	LV1-LV3: 1 (15%)
	LV1-LV2: 2 (28%)

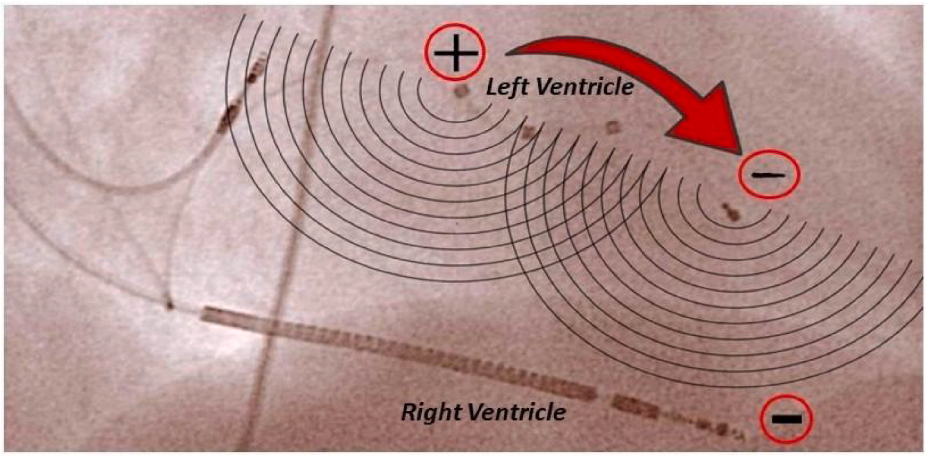

Fig. 2. During CRT, a beneficial anodal left ventricular (LV) stimulation, simultaneous to the cathodic stimulation, can be demonstrated using a bipolar (or preferably quadripolar) LV lead in which the proximal and distal electrodes serve as the anode and the cathode, respectively, interfacing and depolarizing the myocardium.

Table 2
Summary of electrode sites (Fig. 1) for each patient and pacing configuration. (C) Denotes the cathode, whereas (A) the anode.

PATIENT ID	RVS	S-BS	CC-BS	CA-BS
1	RV (C)	RV (C) + LV1 (C)	RV (C) + LV1 (C) + LV2 (C)	RV (C) + LV1 (C) + LV2 (A)
2	RV (C)	RV (C) + LV1 (C)	RV (C) + LV1 (C) + LV4 (C)	RV (C) + LV1 (C) + LV4 (A)
3	RV (C)	RV (C) + LV1 (C)	RV (C) + LV1 (C) + LV4 (C)	RV (C) + LV1 (C) + LV4 (A)
4	RV (C)	RV (C) + LV1 (C)	RV (C) + LV1 (C) + LV4 (C)	RV (C) + LV1 (A) + LV4 (C)
5	RV (C)	RV (C) + LV1 (C)	RV (C) + LV1 (C) + LV3 (C)	RV (C) + LV1 (C) + LV3 (A)
6	RV (C)	RV (C) + LV1 (C)	RV (C) + LV1 (C) + LV2 (C)	RV (C) + LV1 (C) + LV2 (A)
7	RV (C)	RV (C) + LV1 (C)	RV (C) + LV1 (C) + LV4 (C)	RV (C) + LV1 (C) + LV4 (A)

mechanical parameters for all patients. We adapt to them only the geometry of the left ventricle and the size and position of scar regions based on echocardiographic data, without performing any sort of parameters tuning due to lack of clinical information.

2. Methods

2.1. Clinical data

The study protocol was reviewed by our Institutional Review Board and was implemented in accordance with the Declaration of Helsinki.

We enrolled seven consecutive patients (Table 1) undergoing CRT device implantation at our hospital for conventional indications (HFrEF with EF $< 35\%$ and left bundle branch block). Two of them, patients #2 and #6, have a scar due to prior myocardial infarction. All patients received a quadripolar LV lead: three from Biotronik (all Sentus OTW model, BiotronikGmbh, Berlin, Germany), two from Boston Scientific (all 4674 ACUITY™ X4 model, Boston Scientific Corp., Marlborough, MA, USA), one from St. Jude (1458Q Quartet model, St. Jude Medical, St. Paul, MN, USA), and one from Medtronic (4298 Attain Performa model, Medtronic, Minneapolis, MN, USA). The LV lead was targeted to a lateral or posterolateral branch of the coronary sinus.

Four different stimulation configurations were tested:

- right ventricular only pacing (right ventricular stimulation: RVS), assuming it as the baseline configuration to make the baseline heart rate comparable among the patients;
- *conventional* single point CRT (Single Point Biventricular Stimulation: S-BS): The pacing sensing analyzer (PSA) atrial channel is connected in the standard bipolar configuration to atrial lead, the ventricular channel anode is connected to RV lead anode (ring), and the ventricular channel PSA cathode is connected to RV lead cathode (tip) and LV chosen stimulation pole;
- MPP CRT (Multipoint Biventricular Stimulation: CC-BS): The PSA atrial channel is connected in the standard bipolar configuration to the atrial lead, the ventricular channel anode is connected to the RV lead anode (ring), and the ventricular channel PSA cathode is connected to the RV lead cathode (tip) and LV chosen two stimulation poles (i.e. 1 and 4);
- Cathodic-anodal CRT (Cathodic-Anodal Stimulation: CA-BS): The PSA atrial channel is connected in a standard bipolar configuration to the atrial lead, the ventricular channel PSA cathode is connected to the RV lead cathode (tip) and LV chosen stimulation pole (i.e. 1), and the ventricular channel PSA anode is connected to the LV chosen pole (i.e. 4).

See Fig. 1 for a schematic representation of electrodes position and Fig. 2 for the cathodic-anodal stimulation. In Table 2, we report a summary of electrode sites for each patient and pacing configuration.

In all configurations, we set the heart rate at 90 *bpm* to overdrive the intrinsic pacing. Moreover, for each stimulation protocol, dual chamber-pacing (DDD mode, with CRT in biventricular stimulation protocols) was applied to patients in sinus rhythm, whereas we used single chamber pacing (VVI mode, with CRT in biventricular stimulation protocols) in the presence of atrial fibrillation. All pacing protocols were delivered for 1 min before recording data; electrical and hemodynamic parameters were averaged over 16 consecutive beats. When pacing was delivered in DDD mode, we used an AV (atrioventricular) interval of 100 ms to ensure full ventricular capture; the VV (interventricular) interval was 0 by definition and per configuration used (that provided simultaneous pacing from all the ventricular cathode/anodes connected). An output at least twice the highest of the measured capture threshold (in cathodic and anodal configuration) was used.

The selection process of the LV lead electrodes (i.e., LV1, LV2, LV3, LV4, see Fig. 1) started by assessing unipolar cathodic and anodal threshold capture for each lead. The cathodic threshold was assessed by connecting the cathode to the chosen LV pole and the anode to the skin; the anodal threshold was assessed with the reverse configuration (anode on the chosen LV pole, cathode on the skin). The reason for proceeding in this way is to obtain both the anodal and the cathodic pacing threshold for each of the electrodes, to be sure that the output used in bipolar configuration would determine the capture of both the electrodes. The validation of this method to ensure *real* anodal capture was already published in a previous paper [17]. Then we selected the most distant electrodes that were both able of cathodic threshold for CC-BS stimulation and one of which at least able of anodic capture for CA-BS stimulation. The assumption is that the larger the dipole, the flatter is depolarization wavefront, ensuring a more effective myocardial capture.

The effect of different biventricular pacing configurations (S-BS, CC-BS and CA-BS) was confirmed by monitoring the surface electrocardiogram throughout the pacing protocols.

During each implant we obtained 12-lead ECG recordings (filter range, 0.15100 Hz; AC filter, 60 Hz, velocity speed 100 mm/s, 10 mm/mV) and compared QRS duration during RVS, S-BS, CC-BS, CA-BS. QRS duration was defined as the time measured from the earliest ventricular deflection until the last return to the isoelectric line in any lead. All ECG measurements were automatically recorded and subsequently manually reviewed by an expert cardiologist blinded to all patients' characteristics. Minimally invasive hemodynamic assessment by radial artery catheterization using Pressure Recording Analytical Method (PRAM) by Most Care (Vytech Health, Padova, Italy) processed the following parameters for each pacing configuration:

- **dPdt**$_{max}$ (mmHg/ms);
- systolic arterial pressure (**P**$_{sys}$, mmHg);
- stroke volume (**SV**: ml).

PRAM was first proposed and validated in Ref. [45], where the authors simultaneously estimated cardiac output by the direct-oxygen Fick method, Thermodilution (ThD) by means of the pulmonary artery catheter (PAC), and PRAM. A very good correlation was found between PRAM and both the Fick method and ThD. In subsequent studies [4,38,44], the PRAM technique was also validated under several clinical conditions and a strong correlation between the minimally invasive hemodynamic assessment by radial artery measurements and the invasive LV/aorta direct measurements was demonstrated. Transthoracic echocardiography was performed before the procedure for each patient: telediastolic and telesistolic left ventricular longitudinal and transverse diameter by apical view (four-chamber apical view, five-chamber apical view and two-chamber apical view) was obtained to guide the creation of the electroanatomical model.

2.2. Statistical analysis

Descriptive statistics are reported as means and standard deviations (SD) for normally distributed continuous variables or median values with interquartile range in the case of skewed distribution. Differences between mean data were compared using the *t*-test for Gaussian variables. The Mann-Whitney test and Wilcoxon nonparametric test were used to compare non-Gaussian variables for independent and paired samples, respectively. Statistical significance was assumed at $p < 0.05$. All statistical analysis was performed by means of STATISTICA software, version 7.1 (StatSoft, Inc.,Tulsa, OK, USA).

2.3. Mathematical models

The numerical simulations are based on the cardiac electromechanical coupling (EMC) model [12,13,26,53]. This model describes the interplay between the spread of electrical excitation in the cardiac tissue and the consequent contraction-relaxation process. The EMC model consists of four subcomponents, two for the bioelectrical activity and two for the mechanical response of the cardiac tissue.

a) **Mechanical model of cardiac tissue.** The deformation of the cardiac tissue is described by the equations of three-dimensional nonlinear elasticity

$$\mathrm{Div}(\mathbf{FS}) = \mathbf{0}, \qquad \mathbf{X} \in \widehat{\Omega}, \tag{1}$$

where $\mathbf{X} = (X_1, X_2, X_3)^T$ are the material coordinates of the undeformed cardiac domain $\widehat{\Omega}$ ($\mathbf{x} = (x_1, x_2, x_3)^T$ are the spatial coordinates of the deformed cardiac domain $\Omega(t)$ at time t), Div denotes the divergence operator in the reference configuration and $\mathbf{F}(\mathbf{X}, t) = \frac{\partial \mathbf{x}}{\partial \mathbf{X}}$ is the deformation gradient. The second Piola-Kirchoff stress tensor $\mathbf{S} = \mathbf{S}^{pas} + \mathbf{S}^{vol} + \mathbf{S}^{act}$ is assumed to be the sum of passive, volumetric and active components. The passive and volumetric components are defined as

$$S_{ij}^{pas,vol} = \frac{1}{2}\left(\frac{\partial W^{pas,vol}}{\partial E_{ij}} + \frac{\partial W^{pas,vol}}{\partial E_{ji}}\right) \quad i,j = 1,2,3, \tag{2}$$

where $\mathbf{E} = \frac{1}{2}(\mathbf{C} - \mathbf{I})$ and $\mathbf{C} = \mathbf{F}^T\mathbf{F}$ are the Green-Lagrange and Cauchy strain tensors, W^{pas} is an exponential strain energy function (derived from Refs. [19,22]) modeling the myocardium as a transversely isotropic hyperelastic material, i.e.

$$W^{pas} = \frac{a}{2b}(e^{b(I_1-3)} - 1) + \frac{a_l}{2b_l}\left(e^{b_l(\max\{I_{4l}-1,0\})^2} - 1\right) \tag{3}$$

where $I_1 = \mathbf{C}$: $\mathbf{I}$, $I_{4l} = \mathbf{a}_l^T\mathbf{C}\mathbf{a}_l$, $\mathbf{a}_l$ is the local fiber direction, and $W^{vol} = K(J-1)^2$ is a volume change penalization term accounting for the near incompressibility of the myocardium, with K a positive bulk modulus and $J = det(\mathbf{F})$.

b) **Mechanical model of active tension.** The active component of the stress tensor is given by $\mathbf{S}^{act} = T_a\frac{\mathbf{a}_l \otimes \mathbf{a}_l}{\mathbf{a}_l^T\mathbf{C}\,\mathbf{a}_l}$, where $T_a = T_a\left(Ca_i, \lambda, \frac{d\lambda}{dt}\right)$ is the fiber active tension, obtained by solving a biochemical differential system depending on intracellular calcium concentrations, the myofiber stretch $\lambda = \sqrt{\mathbf{a}_l^T\mathbf{C}\mathbf{a}_l}$ and stretch-rate $\frac{d\lambda}{dt}$ (see Ref. [26]).

c) **Bioelectrical model of cardiac tissue: the Bidomain model.** The bioelectrical components considered in this study are the Bidomain model for the electrical current flow, including also the presence of ischemic regions [13,24,54], and the ten Tusscher human ventricular model [52] for the cellular membrane dynamics. We recall that the Bidomain model allows to elicit cardiac excitation from the anodal leads included in our CRT protocol, see Refs. [10,11,41,47,48,55].

The evolution of the cardiac extracellular and transmembrane potentials u_e, v, gating variable $\mathbf{w}$, and ionic concentrations $\mathbf{c}$, is given by the Bidomain model. In the Lagrangian framework, after the pull-back on the reference configuration $\widehat{\Omega} \times (0, T)$, the Bidomain system reads

$$\begin{cases} c_m J\ \dfrac{\partial v}{\partial t} - \mathrm{Div}(J\ \mathbf{F}^{-1}D_i\mathbf{F}^{-T}\mathrm{Grad}(v + u_e)) + J\ i_{ion}(v, \mathbf{w}, \mathbf{c}, \lambda) = J\ i_{app} \\ -\mathrm{Div}(J\ \mathbf{F}^{-1}D_i\mathbf{F}^{-T}\mathrm{Grad}v) - \mathrm{Div}(J\ \mathbf{F}^{-1}(D_i + D_e)\mathbf{F}^{-T}\mathrm{Grad}u_e) = 0, \end{cases} \tag{4}$$

where c_m and i_{ion} are the membrane capacitance and ionic current per unit volume, respectively; see Ref. [13] for the detailed derivation. These two partial differential equations (PDEs) are coupled through the reaction term i_{ion} with the ODE system of the membrane model, given in $\Omega(t) \times (0, T)$ by

$$\frac{\partial \mathbf{w}}{\partial t} - \mathbf{R}_w(v, \mathbf{w}) = 0, \quad \frac{\partial \mathbf{c}}{\partial t} - \mathbf{R}_c(v, \mathbf{w}, \mathbf{c}) = 0. \tag{5}$$

This system is completed by prescribing initial conditions, insulating

boundary conditions, and the applied current i_{app}. Since the extracellular potential u_e is defined up to a time dependent constant in space, we fix it by imposing that u_e has zero average on the cardiac domain; see Ref. [13] for further details. The transversely isotropic conductivity tensors in the deformed configuration are given by

$$D_{i,e} = \sigma_t^{i,e}\, I + (\sigma_l^{i,e} - \sigma_t^{i,e})\mathbf{a}_l \otimes \mathbf{a}_l, \tag{6}$$

where $\sigma_l^{i,e}$, $\sigma_t^{i,e}$ are the conductivity coefficients in the intra- and extracellular media measured along and across the fiber direction $\mathbf{a}_l$, $\mathbf{a}_t$.

d) **Ionic membrane model and stretch-activated channel current.** The ionic current in the Bidomain model (4) is $i_{ion} = \chi I_{ion}$, where χ is the membrane surface to volume ratio and $I_{ion}(v, \mathbf{w}, \mathbf{c}, \lambda) = I_{ion}^m(v, \mathbf{w}, \mathbf{c}) + I_{sac}(v, \mathbf{c}, \lambda)$ is the sum of the ionic term $I_{ion}^m(v, \mathbf{w}, \mathbf{c})$ given by the ten Tusscher model (TP06) consisting of 17 ordinary differential equations [52], available from the cellML depository (models.cellml.org/cellml), and a stretch-activated current I_{sac}. In this work, we adopt the model of I_{sac} proposed in Ref. [32] as the sum of nonselective and selective currents $I_{sac} = I_{ns} + I_{Ko}$. For further details, we refer to Ref. [13].

e) **Pressure-volume loop model.** The intracavitary blood pressure P_{LV} in the left ventricular (LV) cavity is described by a pressure-volume loop model, as in Ref. [19], based on the following four phases:

1. Isovolumetric LV contraction phase, where P_{LV} increases from the end diastolic pressure (EDP) value of about 1.8 kPa–10 kPa;
2. Ejection phase, where the pressure-volume relationship is described by a two element Windkessel model, until the volume reduction stops;
3. Isovolumetric LV relaxation phase, where P_{LV} decreases to 1 kPa;
4. Filling phase, where P_{LV} increases linearly to EDP.

For further details regarding the EMC model, see Ref. [13]. Since the pressure-volume loop model adopted does not provide the arterial blood pressure, we compute the *in silico* $\mathbf{dPdt}_{max}$ and $\mathbf{P}_{sys}$ parameters from P_{LV}.

2.4. Numerical methods

Space discretization. The computational domain is a truncated ellipsoid representing the LV geometry. The sizes of the major and minor axis of the ellipsoid are tuned to match the dimension of the patients' LV dimensions. We discretize the LV domain with a hexahedral structured grid T_{h_m} for the mechanical model (1) and T_{h_e} for the Bidomain model (4), where T_{h_e} is a refinement of T_{h_m}, i.e. h_m is an integer multiple of h_e. We consider the variational formulations of both mechanical and bioelectrical models and then approximate all scalar and vector fields by isoparametric Q_1 finite elements in space. In all the electromechanical simulations, we employ an electrical mesh size of about $h_e = 0.02$ cm to properly resolve the sharp excitation front, while the smoother mechanical deformation allows us to use a coarse mechanical mesh size of about $h_m = 0.16$ cm. The resulting electrical mesh consists of 3, 631, 488 nodes, whereas the mechanical mesh has 8, 400 nodes.

Time discretization. The time discretization of the electromechanical model is performed by the following semi-implicit splitting method, where the electrical and mechanical time steps could be different. At each time step:

a) given v^n, w^n, c^n at time t_n, solve the ODE system of the membrane model (5) with a first order implicit-explicit (IMEX) method to compute the new w^{n+1}, c^{n+1};
b) given the calcium concentration Ca_i^{n+1}, which is included in the concentration variables c^{n+1}, solve the variational formulation of the mechanical problem (1) and the active tension system to compute the new deformed coordinates $\mathbf{x}^{n+1}$, providing the new deformation gradient tensor $\mathbf{F}_{n+1}$;
c) given w^{n+1}, c^{n+1}, $\mathbf{F}_{n+1}$ and $J_{n+1} = \det(\mathbf{F}_{n+1})$, solve the variational formulation of the Bidomain system (4) with a first order IMEX method and compute the new electric potentials v^{n+1}, u_e^{n+1} with an operator splitting method, consisting of decoupling the parabolic from the elliptic equation.

In our simulations, the electrical time step size is $\Delta_e t = 0.05$ ms, while the mechanical times step is $\Delta_m t = 0.25$ ms. Our parallel Fortran90 code is based on the PETSc parallel library [6]. The simulations were run on 256 cores of the Linux cluster Marconi of the CINECA laboratory (www.cineca.it). For further details on the numerical methods and their validation, we refer to Refs. [12,13,16,36].

2.5. Parameters used in numerical simulations

The intra (i-) and extra (e−) cellular conductivity coefficients of the Bidomain model, along (l) and across (t) the fiber direction, are

$$\sigma_l^i = 3,\ \sigma_l^e = 2,\ \sigma_t^i = 0.31525,\ \sigma_t^e = 1.3514,$$

all in $m\Omega^{-1}cm^{-1}$. Using the ten Tusscher human ventricular model [52] for the cellular membrane dynamics and the previous conductivity values, the simulated activation wavefronts propagate along and across the fiber direction with physiological conduction velocities [43]. The parameters of the strain energy function (3) are those given in Ref. [19], except the bulk modulus K, i.e.

$$a = 0.333\ kPa,\ b = 9.242,\ a_l = 18.535\ kPa,\ b_l = 15.972,\ K = 200\ kPa.$$

Scar burden and scar tissue distribution were associated with differences in response to CRT; scar tissue can modify the propagation of the electrical wavefront of ventricular activation and jeopardize the effect of resynchronization, leading to a lack of favorable remodeling [21,50]. However, in the acute setting, in an intra-patient comparison between different pacing configurations, this effect was considered negligible: the same scar burden and distribution were responsible for the hemodynamic responses with subsequent pacing protocols. To verify whether our model could approximate the real *clinical* response, we tried to include scar tissue in our simulation, including it according to scar localization as detected by preprocedural echocardiography.

For the LV models of patients #2 and #6, we locate the scar region based on the echocardiographic data. The scar is assumed to develop along the whole transmural thickness, from the endocardial to the epicardial surface. From the bioelectrical point of view, scar tissue is assumed to have passive membrane properties, with a conductance of 0.01F/A. The intracellular conductivity values are decreased by 90% in both the along and cross fiber directions. Extracellular tissue is assumed to be isotropic with a conductivity of 0.5 $m\Omega^{-1}\mathrm{cm}^{-1}$. From the mechanical point of view, scar tissue is modeled by reducing the active tension and passive tissue stiffness by 10% and 25% with respect to their normal values, respectively.

We note that the previous conservative set of electrophysiological and mechanical parameters is used for all seven patients. Therefore, in our simulation study, we have not considered parameters tuning and patient specific optimization, but the macroscopic dimensions of each patient's left ventricle (height, diameter, cavity and scar region size) have been taken into account using transthoracic echocardiography.

The excitation process is initiated by stimulating the exterior surface of the half of the LV geometry corresponding to the septum (RVS stimulation) and the epicardial surface of the other half in one (S-BS) or two (CC-BS and CA-BS) sites, with the position depending on the electrode's position of the corresponding patient. See Fig. 1 for a schematic representation of the position of the electrodes. In RVS, S-BS and CC-BS stimulations, all pacing electrodes are cathodes. To model a cathodic stimulation, we apply in the Bidomain model a positive intracellular current and a negative extracellular current in the same small tissue volume to induce a depolarizing transmembrane current. In CA-BS

Table 3
Hemodynamic parameters (**SV**, **dPdt**$_{max}$, **P**$_{sys}$) and **QRS** measured from the seven patients. The last four rows contain the corresponding average and standard deviation values on the seven patients. Boldface fonts indicate values that are significantly ($p \leq 0.01$) different from the reference RVS value.

ID-STIM	SV	dPdt$_{max}$	P$_{sys}$	QRS
	(ml)	(mmHg/ms)	(mmHg)	(ms)
1-RVS	43	0.79	133	165
1-S-BS	42	0.77	131	126
1-CC-BS	40	0.74	128	120
1-CA-BS	36	0.75	126	117
2-RVS	65	1.22	142	180
2-S-BS	86	1.37	153	141
2-CC-BS	60	1.21	140	148
2-CA-BS	69	1.19	153	153
3-RVS	40	0.51	117	184
3-S-BS	44	0.67	142	120
3-CC-BS	42	0.63	136	114
3-CA-BS	44	0.64	138	112
4-RVS	55	0.81	103	150
4-S-BS	27	0.80	102	120
4-CC-BS	26	0.78	99	116
4-CA-BS	27	0.77	99	109
5-RVS	39	0.74	127	165
5-S-BS	41	0.76	128	136
5-CC-BS	39	0.73	125	136
5-CA-BS	39	0.76	124	132
6-RVS	35	0.84	124	150
6-S-BS	30	0.79	117	135
6-CC-BS	46	0.79	118	132
6-CA-BS	38	0.71	112	132
7-RVS	35	0.48	88	155
7-S-BS	35	0.57	95	129
7-CC-BS	38	0.65	105	123
7-CA-BS	33	0.62	101	126
RVS	45 ± 11	0.77 ± 0.25	119 ± 18	164 ± 14
S-BS	44 ± 20	0.82 ± 0.26	124 ± 21	**130** ± 8
CC-BS	42 ± 20	0.79 ± 0.19	122 ± 15	**127** ± 12
CA-BS	41 ± 13	0.78 ± 0.19	122 ± 20	**126** ± 15

Table 4
Hemodynamic parameters (**SV**, **dPdt**$_{max}$, **P**$_{sys}$) and duration of left ventricle activation (**TAT**) computed from numerical simulations. The last four rows contain the corresponding average and standard deviation values on the seven patient models. Boldface fonts indicate values that are significantly ($p \leq 0.01$) different from the reference RVS value.

ID-STIM	SV	dPdt$_{max}$	P$_{sys}$	TAT
	(ml)	(mmHg/ms)	(mmHg)	(ms)
1-RVS	35	0.55	100	177
1-S-BS	40	0.64	107	130
1-CC-BS	36	0.66	106	130
1-CA-BS	37	0.65	106	129
2-RVS	34	0.43	96	184
2-S-BS	37	0.61	102	128
2-CC-BS	37	0.56	99	129
2-CA-BS	37	0.57	99	128
3-RVS	34	0.28	89	167
3-S-BS	37	0.50	97	124
3-CC-BS	37	0.48	93	125
3-CA-BS	37	0.47	93	124
4-RVS	39	0.42	96	167
4-S-BS	43	0.54	103	117
4-CC-BS	42	0.53	102	117
4-CA-BS	42	0.52	101	117
5-RVS	39	1.10	148	238
5-S-BS	54	1.23	163	165
5-CC-BS	56	1.22	164	166
5-CA-BS	56	1.20	164	164
6-RVS	36	0.81	95	179
6-S-BS	42	0.76	109	129
6-CC-BS	41	0.69	108	129
6-CA-BS	41	0.71	108	130
7-RVS	31	1.04	123	206
7-S-BS	42	1.14	132	138
7-CC-BS	48	1.15	132	138
7-CA-BS	47	1.16	133	139
RVS	35 ± 3	0.66 ± 0.32	107 ± 21	188 ± 26
S-BS	**42** ± 6	**0.77** ± 0.29	**116** ± 23	**133** ± 15
CC-BS	**42** ± 7	**0.76** ± 0.30	**115** ± 25	**133** ± 16
CA-BS	**42** ± 7	**0.75** ± 0.30	**115** ± 25	**133** ± 15

stimulation, supposing, for instance, that LV1 is the cathode and LV2 is the anode, we apply a negative extracellular current in a small tissue volume in the LV1 location and a positive extracellular current in a small tissue volume in the LV2 location, such that the total applied current is zero. The portion of tissue where the current is applied is a cubic volume with an edge of approximately 0.04 cm. The value of applied current is about twice the threshold. For each simulation, the simulated time span is 500 ms. The computational cost required by the single simulation is about 10 h.

As an estimate of the **QRS** duration, we compute the duration of LV electrical activation (**TAT**), defined as the maximum minus the

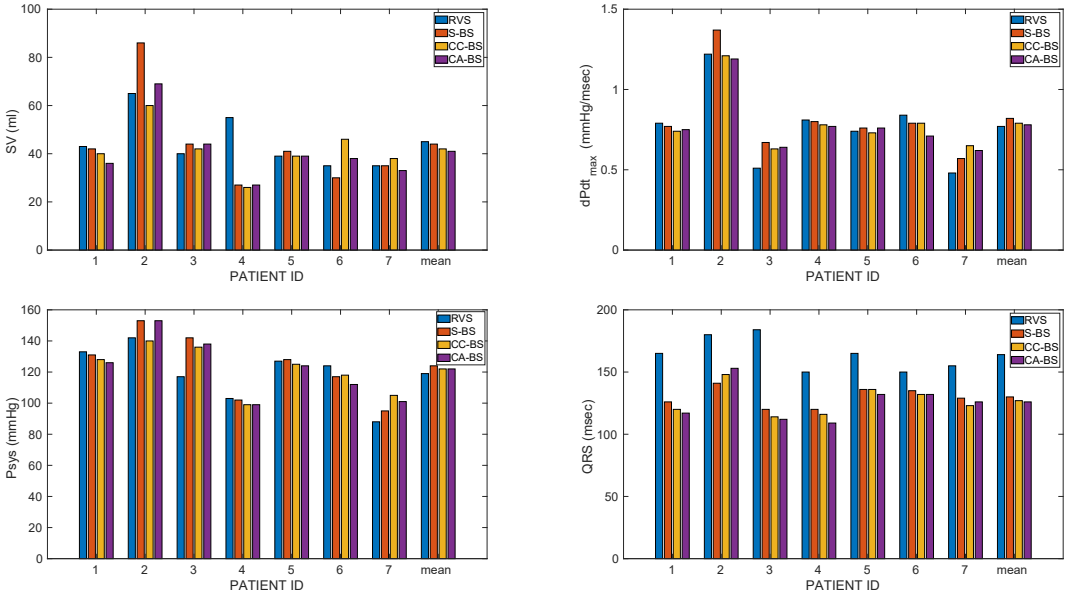

Fig. 3. Clinical data: Bar plots of **SV**, **dPdt**$_{max}$, **P**$_{sys}$ and **QRS** computed from the seven patients.

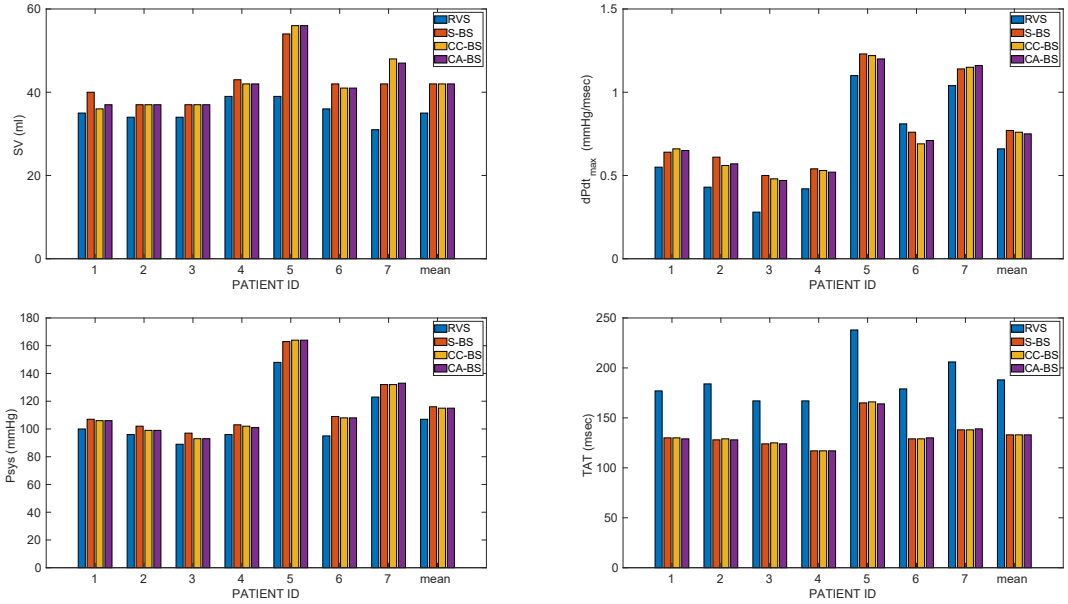

Fig. 4. Numerical simulations: Bar plots of **SV**, $\mathbf{dPdt}_{max}$, $\mathbf{P}_{sys}$ and **TAT** computed from the seven patients.

minimum local activation time on all the LV computational nodes. Local activation time is computed in each LV node as the instant of maximum time derivative during the depolarization phase of the action potential waveform.

3. Results

3.1. Clinical data

Table 1 reports the clinical characteristics of the seven patients, whereas Table 2 reports a summary of electrode sites for each patient and pacing configuration. Table 3 reports the hemodynamic parameters (**SV**, $\mathbf{dPdt}_{max}$, $\mathbf{P}_{sys}$) and the **QRS** duration computed from experiments on the seven patients, who underwent the four stimulation protocols RVS, S-BS, CC-BS and CA-BS. With respect to the RVS stimulation, the S-BS stimulation exhibits, although not statistically significant, an average slight decrease of **SV** (from 45 ± 11 to 44 ± 10 ml), a 6% increase of $\mathbf{dPdt}_{max}$ (from 0.77 ± 0.25 to 0.82 ± 0.26 mmHg/ms) and a 4% increase of $\mathbf{P}_{sys}$ (from 119 ± 18 to 124 ± 21 mmHg). Regarding the electrical activation, ventricular excitation elicited by S-BS stimulation results significantly faster than RVS ($p = 0.001$), because **QRS** duration reduces from 164 ± 14 (RVS) to 130 ± 8 ms (S-BS). The hemodynamic parameters associated with the CC-BS stimulation do not show any significant improvement with respect to the S-BS one, since they result all slightly reduced. Moreover, all the hemodynamic parameters of the CC-BS and CA-BS stimulation protocols are comparable. Considering ventricular

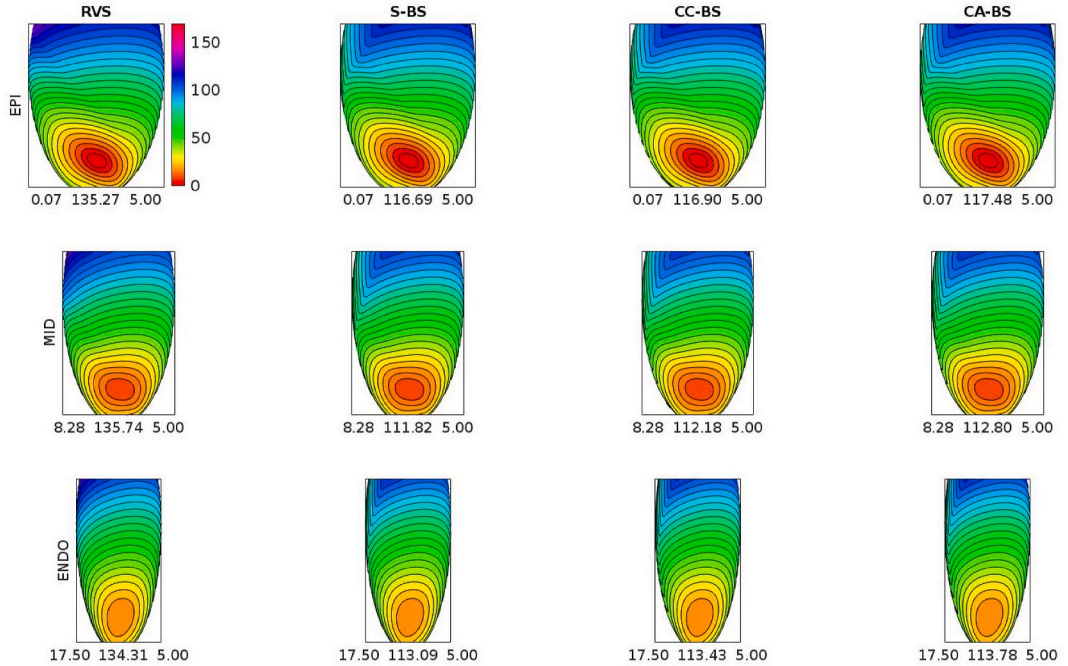

Fig. 5. Activation time isochrones computed from RVS, S-BS, CC-BS and CA-BS numerical simulations, displayed on the half of the LV model of patient #4 corresponding to the septum. Below each plot, the minimum, maximum and step (all in *ms*) of the displayed map are reported.

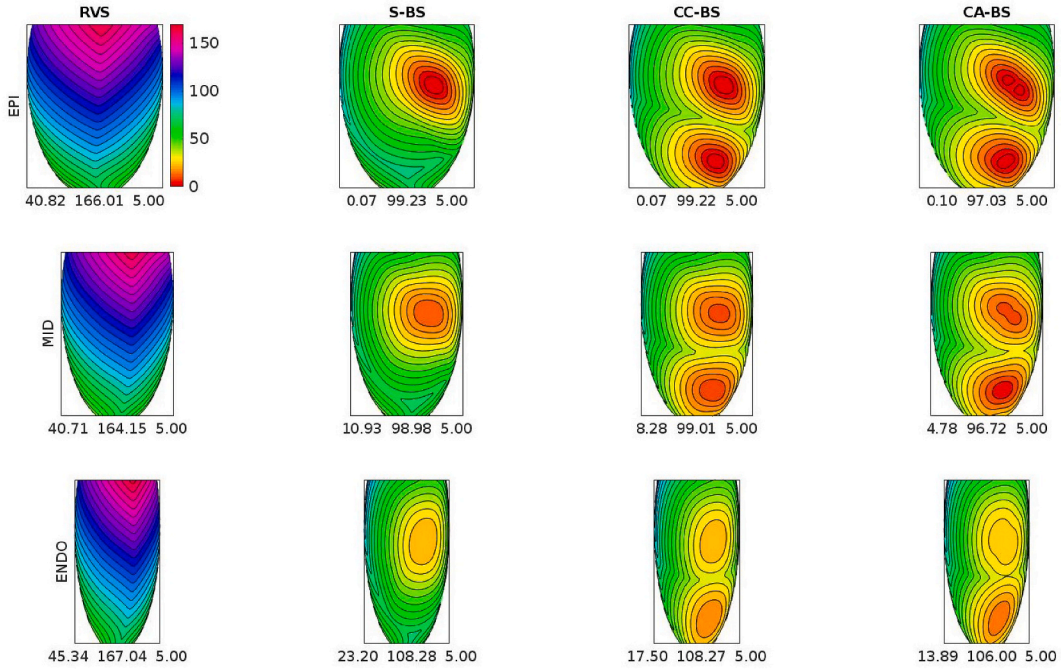

Fig. 6. Activation time isochrones computed from RVS, S-BS, CC-BS and CA-BS numerical simulations, displayed on the half of the LV model of patient #4 corresponding to the postero-lateral side. In CA-BS, LV1 is the anode and LV4 is the cathode. Below each plot, the minimum, maximum and step (all in *ms*) of the displayed map are reported.

activation, **QRS** duration reduced significantly from RVS to CC-BS (127 ± 12 ms, p = 0.001) and CA-BS (126 ± 15 ms, p = 0.001), but there were no electrical differences between each biventricular configuration. Fig. 3 reports the bar plots of **SV**, $\mathbf{dPdt}_{max}$, $\mathbf{P}_{sys}$ and **QRS** computed from each of the seven patients. The bar plots highlight that no significant differences arise among the S-BS, CC-BS and CA-BS stimulations.

3.2. Numerical simulations

Table 4 reports the hemodynamic parameters (**SV**, $\mathbf{dPdt}_{max}$, $\mathbf{P}_{sys}$) and **TAT** computed from the numerical simulations on the LV models of the seven patients. With respect to the RVS stimulation, the S-BS stimulation exhibits: a significant **SV** average increase of about 17% (from 35 ± 3 to 42 ± 6 ml, p = 0.008); a significant $\mathbf{dPdt}_{max}$ average increase of about 17% (from 0.66 ± 0.32 to 0.77 ± 0.29 mmHg/ms, p = 0.01); a significant $\mathbf{P}_{sys}$ average increase of about 8% (from 107 ± 21 to 116 ± 23 mmHg, p = 0.0004). The S-BS, CC-BS and CA-BS stimulations instead exhibit comparable performances in terms of all hemodynamic parameters. The LV **TAT** reduces significantly from RVS (188 ± 25 ms) to each biventricular stimulation (118 ± 15 ms, p < 0.001 for S-BS; 127 ± 15 ms, p = 0.0004 for CC-BS; 125 ± 15 ms, p = 0.0005 for CA-BS), whereas there were no significant differences among biventricular configurations.

In Fig. 4, we report for completeness the bar plots of **SV**, $\mathbf{dPdt}_{max}$, $\mathbf{P}_{sys}$ and **TAT** computed from the LV models of the seven patients. The bar plots confirm that no significant differences arise among the S-BS, CC-BS and CA-BS stimulations.

As an example of activation sequences, we report in Figs. 5–7 the activation time isochrones computed from the LV model of patient #4, for each of the stimulation protocols. Analogous activation maps for the ischemic patient #6 are reported in the data supplement. We note that in CA-BS the excitation wavefront elicited by the LV1 lead (anode) starts from the two virtual cathodes, see Fig. 6 (top-right panel). On the half of the LV model corresponding to the postero-lateral side, although the S-BS and CC-BS activation sequences present some differences, their total activation times are comparable on all the endocardial, midmyocardial and epicardial surfaces. This similarity is also confirmed by the unipolar electrogram waveforms computed from the epicardial postero-lateral side and reported in Fig. 8. The waveforms generated by the S-BS and CC-BS stimulations exhibit similar morphology, and especially in the basal regions they are almost superimposed. Analogous considerations hold for the fiber strains computed in the same locations (Fig. 9). This could explain why the contraction phases triggered by the S-BS and CC-BS stimulations yield comparable hemodynamic outcomes.

4. Discussion

The present investigation is two-fold. First, we have performed a clinical study on the effectiveness of bicathodic multipoint pacing (CC-BS) and cathodic-anodal pacing (CA-BS) CRT, with respect to conventional biventricular (S-BS) CRT, in terms of the following hemodynamic parameters: stroke volume (**SV**), maximal arterial pressure slope ($\mathbf{dPdt}_{max}$) and systolic arterial pressure ($\mathbf{P}_{sys}$). A cohort of seven patients underwent CRT.

Then, from the geometric data of the LV of the seven patients, we have constructed seven LV geometric models and run electromechanical numerical simulations to compare the *in silico* hemodynamic and electrical parameters with those obtained from the patients. The mathematical model consists of a strongly coupled Bidomain electromechanical coupling model, considering the major features of the ventricular structure, such as fiber anisotropy and almost-incompressibility, and a detailed excitation-contraction coupling model, together with mechano-electric feedback. In addition, in case of ischemic cardiomyopathy (patient #2 and #6 of our study), a detailed location of scar region based on *in vivo* echocardiographic data, was performed.

Both *in vivo* and *in silico* results have shown that:

- the multipoint stimulations (CC-BS and CA-BS) do not yield a clear CRT improvement with respect to conventional biventricular pacing (S-BS);
- CC-BS and CA-BS yield comparable CRT performance.

Indeed, the average *in vivo* SV parameter does not improve (i.e.

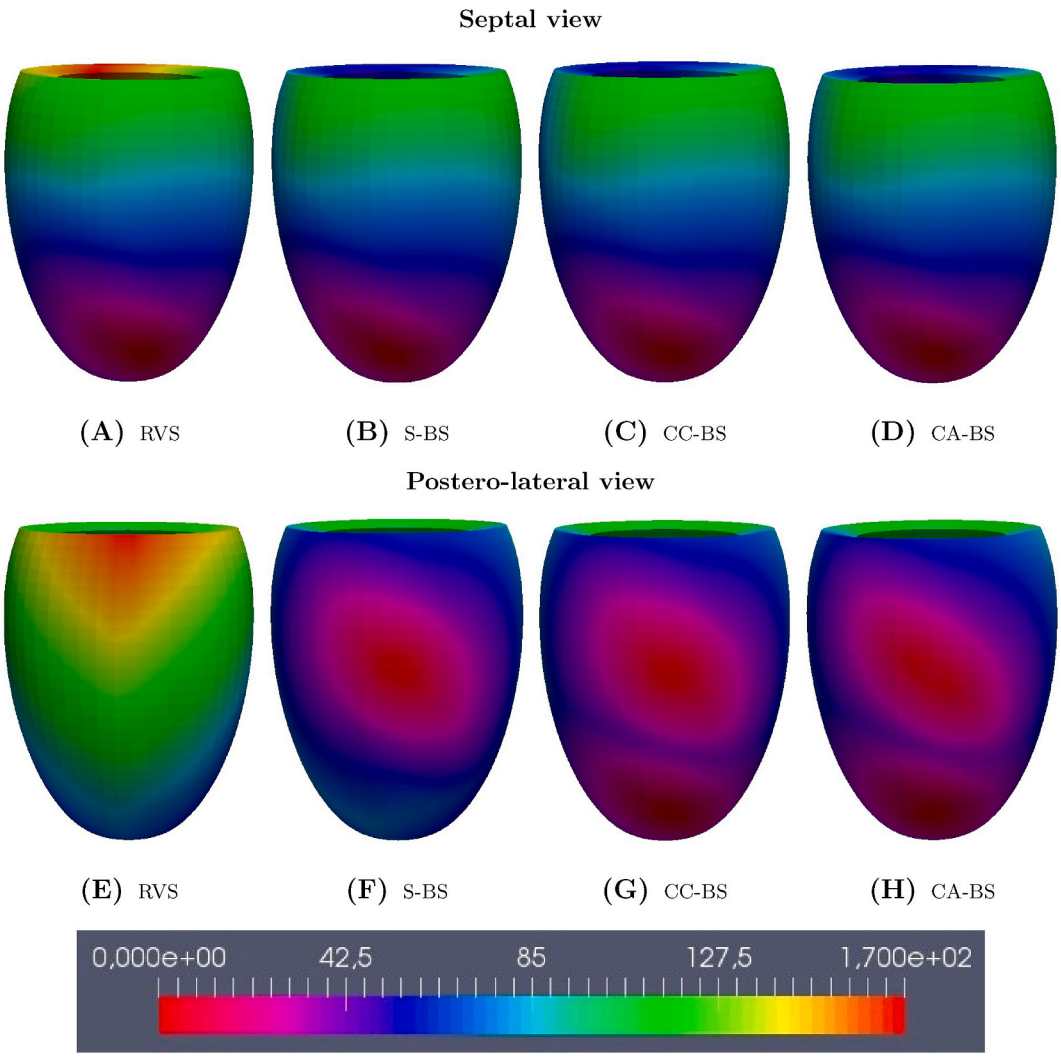

Fig. 7. Three-dimensional distributions of activation time (in *ms*) isochrones computed from RVS, S-BS, CC-BS and CA-BS numerical simulations on patient #4: septal view (first row) and postero-lateral view (second row).

increase) from S-BS (44 ml) to CC-BS (42 ml) and CA-BS (41 ml), and the average *in silico* SV parameter does not improve from S-BS (42 ml) to CC-BS (42 ml) and CA-BS (42 ml). The average *in vivo* **dPdt**$_{max}$ parameter does not improve (i.e. increase) from S-BS (0.82 mmHg/ms) to CC-BS (0.79 mmHg/ms) and CA-BS (0.78 mmHg/ms), and the average *in silico* **dPdt**$_{max}$ parameter does not improve from S-BS (0.77 mmHg/ms) to CC-BS (0.76 mmHg/ms) and CA-BS (0.75 mmHg/ms). The average *in vivo* $\mathbf{P}_{sys}$ parameter does not improve (i.e. increase) from S-BS (124 mmHg) to CC-BS (122 mmHg) and CA-BS (122 mmHg), and the average *in silico* $\mathbf{P}_{sys}$ parameter does not improve from S-BS (116 mmHg) to CC-BS (115 mmHg) and CA-BS (115 mmHg). The average *in vivo* **QRS** parameter does not improve significantly (i.e. decrease) from S-BS (130 ms) to CC-BS (127 ms) and CA-BS (126 mmHg), and the average *in silico* $\mathbf{EAD}_d$ parameter does not improve from S-BS (133 ms) to CC-BS (133 ms) and CA-BS (133 ms).

These findings are in partial disagreement with some previous studies ([34,42,56]), but similar results have been reported in a previous numerical study on a single ventricular geometry [31].

We note that to model the anodal stimulation in CA-BS an essential requirement is the use of the Bidomain model of electrocardiology [10,11,41,47,48,55] instead of the Monodomain model, used e.g. in Ref. [15] for multipoint cathodic CRT simulations.

The comparison between the *in silico* data (Table 4 and Fig. 4) and the *in vivo* data (Table 3 and Fig. 3) shows discrepancies for some specific patients. This was expected, because, due to lack of information, we have not undertaken any tuning procedure of the model parameters on the single patient, but we used the same conservative values of electrical and mechanical parameters for all patients. We have only calibrated the LV geometry of each patient, roughly generated using the ellipsoidal coordinates, based on the echocardiographic measurements. Furthermore, a schematization of the scar geometry was adopted for the two ischemic patients. Thus, our simulations are not patient-specific. Nevertheless all the reported *in silico* output values are in the physiological range and exhibit a good quantitative agreement with the associated *in vivo* parameters. Indeed, the mean (among stimulations) relative error between the average (among patients) *in vivo* parameters and the corresponding average *in silico* parameters is always below 8%.

Despite the aforementioned local discrepancies, the *in vivo* and *in silico* hemodynamic and electrical data exhibit the same global behavior, when the pacing protocol changes from S-BS to CC-BS and CA-BS. We note, however, that, when compared with the baseline RVS stimulation, the *in silico* results related to all biventricular pacing protocols show a significant improvement in the hemodynamic parameters, whereas in the *in vivo* results we failed to demonstrate a statistically significant difference between RVS and biventricular stimulations. On the other hand, we believe that the *in vivo* results are not completetly inconsistent, because they show a trend similar to numerical simulations, in terms of increasing dPdt_{max} and P_{sys}.

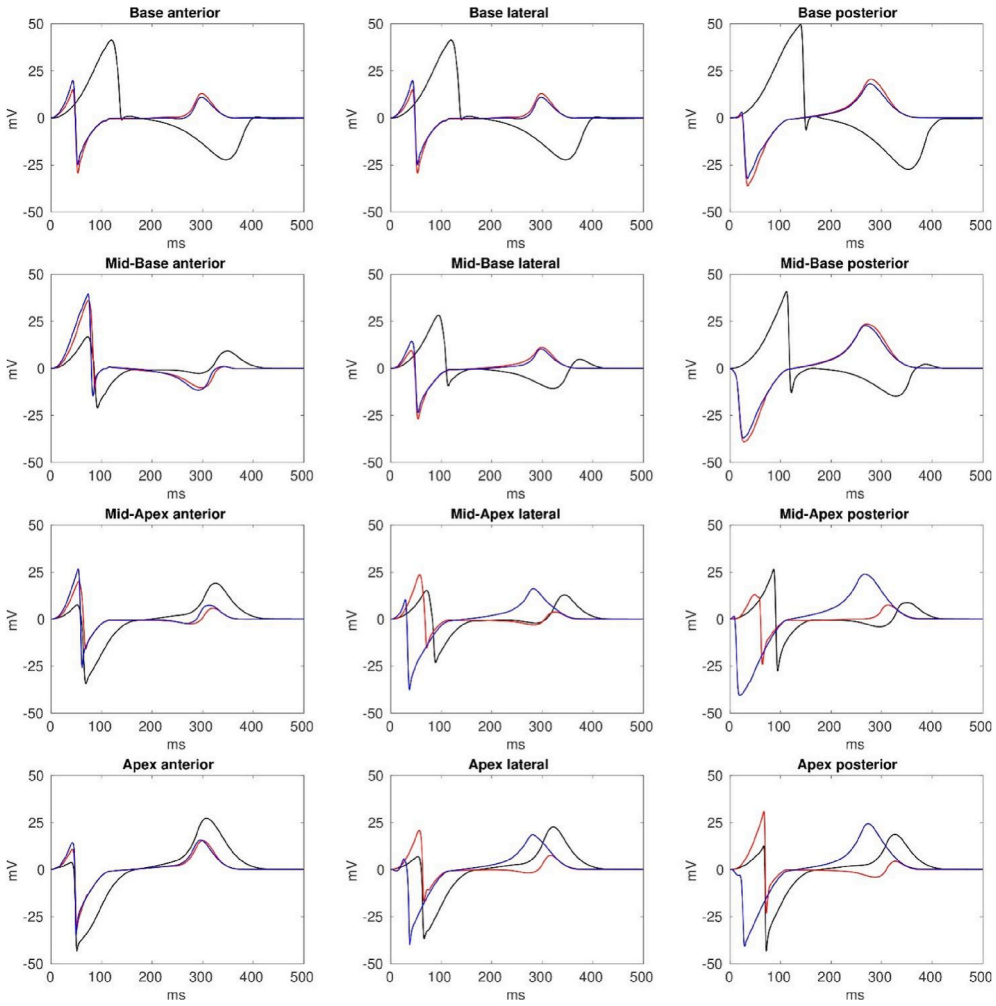

Fig. 8. Unipolar electrograms extracted from 12 epicardial sites located in the half of the LV model of patient #4 corresponding to the postero-lateral side and computed from RVS (black), S-BS (red) and CC-BS(blue) numerical simulations.

Finally, we remark that the only two patients with ischemic regions (#2 and #6) exhibited hemodynamic metrics displaying the same trend of the other patients at varying the CRT protocol. Thus, their inclusion does not affect the average metric reported in Tables 3 and 4 and Figs. 3 and 4, respectively.

4.1. Clinical implications

Our study has confirmed that MPP in CRT remains a controversial issue. Despite the promising preliminary results reported in Refs. [34,42,56], the phase-1 MORE-CRT MPP study [28] showed that MPP does not mean better hemodynamic response in every patient. However, MPP might improve response to therapy in a niche of patients, whose characteristics are not yet defined. Therefore, our results agree with this novel evidence, since they confirm that MPP is not for everyone, neither in the *conventional* form, nor in the cathodic-anodal form. On the seven patients considered, the best improvement in cardiac contractility and hemodynamic parameters with respect to baseline is usually achieved with conventional single point CRT pacing.

Furthermore, concerning the numerical simulations, we note that our aim was not to construct a patient-specific computational tool. We believe that the major importance of our computational results is to provide theoretical support, based on well established mathematical models derived from universal physical principles, to clinical experiments. In this sense, the *in silico* data reported have confirmed the *in vivo* observations.

A further improvement of the computer modeling approach, with the inclusion of a patient-specific calibration of the biventricular and scar geometries, could provide an effective computational tool able to predict the best ventricular stimulation configuration. Starting from *in vivo* individual baseline structural, mechanical and electrical profiles, such computer modeling may help in tailoring CRT to the needs of individual patients, simulating *in silico* the best pacing configuration, which can then be applied *in vivo* to obtain improved resynchronization and to avoid non-response to therapy. Perspective data from an *ad hoc* study are desirable to verify this hypothesis.

4.2. Limitations

The *in vivo* $\mathbf{dPdt}_{max}$ and $\mathbf{P}_{sys}$ parameters were measured by the minimally invasive PRAM technology. Although this technique was extensively validated in previous studies [44], future works should confirm our results using invasive measurements of hemodynamic output at ventricular level. The number of patients analyzed in our study is also limited, but believe that the pool of our patients is sufficient to ascertain (both in the measured and simulated data) the absence of clearly superior performance of the multipoint bicathodic or cathodic-anodal stimulations with respect to the conventional biventricular stimulation. From the computational viewpoint, we have considered transversely isotropic, instead of orthotropic, passive properties of the cardiac tissue and idealized LV geometries, without including the right ventricle. In the two patients with myocardial

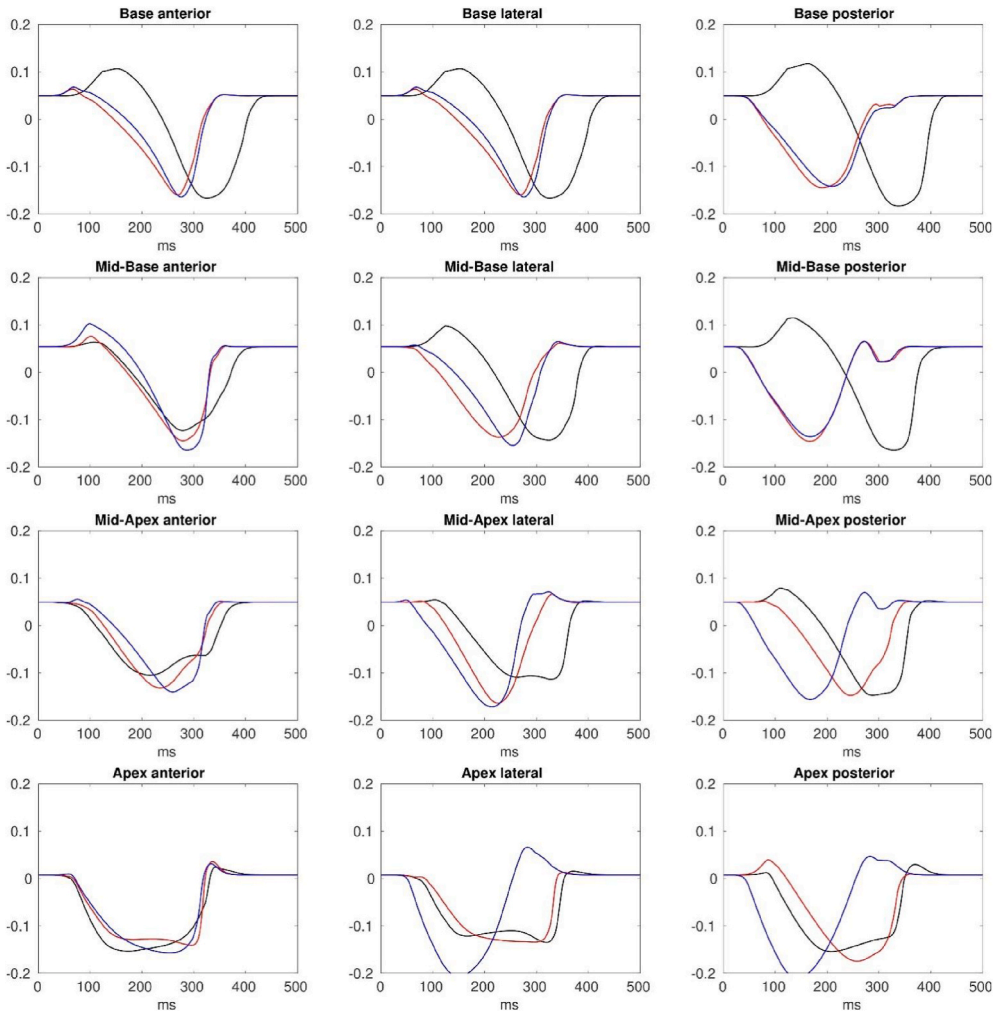

Fig. 9. Fiber strains extracted from 12 epicardial sites located in the half of the LV model of patient 4 corresponding to the postero-lateral side and computed from RVS (black), S-BS (red) and CC-BS (blue) numerical simulations.

infarction, the scar position and extent were modeled only based on echocardiography instead of delay-enhancement MRI, without performing a detailed segmentation of the region or a differentiation between border zone and core zone. The position of the leads was fixed and chosen as in the clinical experiments. Thus, we did not study the optimizations of the lead's position with respect to the scar, as done, e.g., in Ref. [29]. We have also neglected the presence of Purkinje network [3,23,27,46]. This might explain that, in the numerical simulations, activation elicited by RVS stimulations is significantly slower than in clinical results. However, in the other stimulations, QRS duration measured from the patients and the total activation time computed from numerical simulations are comparable. Moreover, we could not include information about the electromechanical delay in the model, since it was not available from the clinical data. However, despite these model simplifications, the values of all *in silico* hemodynamic and electrical parameters considered were comparable with *in vivo* values.

Acknowledgments

S. Scacchi has been supported by grants of MIUR (PRIN 2017AXL54F_003) and INdAM-GNCS. P. Colli Franzone has been supported by grants of INdAM-GNCS. L. F. Pavarino has been supported by grants of MIUR (PRIN 2017AXL54F_002) and INdAM-GNCS.

Appendix A. Supplementary data

Supplementary data to this article can be found online at https://doi.org/10.1016/j.compbiomed.2021.104661.

Conflict of interest

None Declared.

References

[1] W.T. Abraham, Cardiac resynchronization therapy for heart failure: biventricular pacing and beyond, Curr. Opin. Cardiol. 17 (4) (2002) 346–352.
[2] M. Albatat, J. Bergsland, H. Arevalo, et al., Multisite pacing and myocardial scars: a computational study, Comput. Methods Biomech. Biomed. Eng. 23 (6) (2020) 248–260.
[3] N. Ali, M.S. Shin, Z. Whinnett, The emerging role of cardiac conduction system pacing as a treatment for heart failure, Curr. Heart Fail. Rep. 17 (5) (August 2020) 288–298.
[4] J.M. Alonso-Iñigo, F.J. Escribá, J.I. Carrasco, et al., Measuring cardiac output in children undergoing cardiac catheterization: comparison between the fick method and PRAM (pressure recording analytical method), Pediatr. Anesth. 26 (11) (2016) 1097–1105.
[5] A.P. Antoniadis, B. Sieniewicz, J. Gould, et al., Updates in cardiac resynchronization therapy for chronic heart failure: Review of multisite pacing, Curr. Heart Fail. Rep. 14 (5) (2017) 376–383.
[6] S. Balay, S. Abhyankar, M.A. Adams, et al., PETSc Users Manual, 2020. ANL-95/11 - Revision 3.14.
[7] M.R. Bristow, A.M. Feldman, L.A. Saxon, Heart failure management using implantable devices for ventricular resynchronization: comparison of medical

therapy, pacing, and defibrillation in chronic heart failure (COMPANION) trial, J. Card. Fail. 6 (3) (2000) 276–285.
[8] A. Bulava, G. Ansalone, R. Ricci, et al., Triple-site pacing in patients with biventricular device—incidence of the phenomenon and cardiac resynchronization benefit, J. Intervent. Card Electrophysiol. 10 (1) (2004) 37–45.
[9] G. Ciconte, Ž. Ćalović, L.C. McSpadden, et al., Multipoint left ventricular pacing improves response to cardiac resynchronization therapy with and without pressure-volume loop optimization: comparison of the long-term efficacy of two different programming strategies, J. Intervent. Card Electrophysiol. 54 (2) (2019) 141–149.
[10] P. Colli Franzone, L.F. Pavarino, S. Scacchi, Exploring anodal and cathodal make and break cardiac excitation mechanisms in a 3d anisotropic bidomain model, Math. Biosci. 230 (2) (2011) 96–114.
[11] P. Colli Franzone, L.F. Pavarino, S. Scacchi, Cardiac excitation mechanisms, wavefront dynamics and strength-interval curves predicted by 3d orthotropic bidomain simulations, Math. Biosci. 235 (1) (2012) 66–84.
[12] P. Colli Franzone, L.F. Pavarino, S. Scacchi, Parallel multilevel solvers for the cardiac electro-mechanical coupling, Appl. Numer. Math. 95 (2015) 140–153.
[13] P. Colli Franzone, L.F. Pavarino, S. Scacchi, Bioelectrical effects of mechanical feedbacks in a strongly coupled cardiac electro-mechanical model, Math. Model Methods Appl. Sci. 26 (1) (2016) 27–57.
[14] J. Constantino, Y. Hu, N.A. Trayanova, A computational approach to understanding the cardiac electromechanical activation sequence in the normal and failing heart, with translation to the clinical practice of CRT, Prog. Biophys. Mol. Biol. 110 (2–3) (2012) 372–379.
[15] A. Crozier, B. Blazevic, P. Lamata, et al., The relative role of patient physiology and device optimisation in cardiac resynchronisation therapy: a computational modelling study, J. Mol. Cell. Cardiol. 96 (2016) 93–100.
[16] F. Del Bianco, P. Colli Franzone, S. Scacchi, et al., Electromechanical effects of concentric hypertrophy on the left ventricle: a simulation study, Comput. Biol. Med. 99 (2018) 236–256.
[17] G. Dell'Era, F. De Vecchi, E. Prenna, et al., Feasibility of cathodic-anodal left ventricular stimulation for alternative multisite pacing, Pacing Clin. Electrophysiol. 41 (6) (2018) 597–602.
[18] K.F. Dendy, B.D. Powell, Y. Cha, et al., Anodal stimulation: an underrecognized cause of nonresponders to cardiac resynchronization therapy, Indian Pacing Electrophysiol J. 11 (3) (2011) 64–72.
[19] T.S.E. Eriksson, A.J. Prassl, G. Plank, et al., Influence of myocardial fiber/sheet orientations on left ventricular mechanical contraction, Math. Mech. Solid 18 (6) (2013) 592–606.
[20] V.G. Fast, A.G. Kléber, Role of wavefront curvature in propagation of cardiac impulse, Cardiovasc. Res. 33 (2) (1997) 258–271.
[21] S.C. Harb, S. Toro, J.A. Bullen, et al., Scar burden is an independent and incremental predictor of cardiac resynchronisation therapy response, Open Heart 6 (2) (July 2019), e001067.
[22] G.A. Holzapfel, R.W. Ogden, Constitutive modelling of passive myocardium: a structurally based framework for material characterization, Phil. Trans. R. Soc. A 367 (1902) 3445–3475, 2009.
[23] E.R. Hyde, J.M. Behar, S. Claridge, et al., Beneficial effect on cardiac resynchronization from left ventricular endocardial pacing is mediated by early access to high conduction velocity tissue, Circulation: Arrhythmia & Electrophysiol. 8 (5) (October 2015) 1164–1172.
[24] X. Jie, V. Gurev, N.A. Trayanova, Mechanisms of mechanically induced spontaneous arrhythmias in acute regional ischemia, Circ. Res. 106 (1) (2010) 185–192.
[25] R.C.P. Kerckhoffs, A.D. McCulloch, J.H. Omens, et al., Effects of biventricular pacing and scar size in a computational model of the failing heart with left bundle branch block, Med. Image Anal. 13 (2) (2009) 362–369.
[26] S. Land, S.A. Niederer, J.M. Aronsen, et al., An analysis of deformation-dependent electromechanical coupling in the mouse heart, J. Physiol. 590 (18) (2012) 4553–4569.
[27] M. Landajuela, C. Vergara, A. Gerbi, et al., Numerical approximation of the electromechanical coupling in the left ventricle with inclusion of the purkinje network, Int. J. Numer. Meth. Biomed. Eng. 34 (7) (2018), e2984.
[28] C. Leclercq, H. Burri, A. Curnis, et al., Cardiac resynchronization therapy non-responder to responder conversion rate in the more response to cardiac resynchronization therapy with MultiPoint pacing (MORE-CRT MPP) study: results from phase i, Eur. Heart J. 40 (35) (2019) 2979–2987.
[29] C. Mendonca Costa, A. Neic, K. Gillette, et al., Left ventricular endocardial pacing is less arrhythmogenic than conventional epicardial pacing when pacing in proximity to scar, Heart Rhythm 17 (8) (August 2020) 1262–1270.
[30] A.J. Moss, W.J. Hall, D.S. Cannom, et al., Cardiac-resynchronization therapy for the prevention of heart-failure events, N. Engl. J. Med. 361 (14) (2009) 1329–1338.
[31] S.A. Niederer, A.K. Shetty, G. Plank, et al., Biophysical modeling to simulate the response to multisite left ventricular stimulation using a quadripolar pacing lead, Pacing Clin. Electrophysiol. 35 (2) (2011) 204–214.
[32] S.A. Niederer, N.P. Smith, A mathematical model of the slow force response to stretch in rat ventricular myocytes, Biophys. J. 92 (11) (2007) 4030–4044.
[33] E. Occhetta, G. Dell'Era, A. Giubertoni, et al., Occurrence of simultaneous cathodal–anodal capture with left ventricular quadripolar leads for cardiac resynchronization therapy: an electrocardiogram evaluation, Europace 19 (4) (2017) 596–601.
[34] C. Pappone, Ž. Ćalović, G. Vicedomini, et al., Multipoint left ventricular pacing improves acute hemodynamic response assessed with pressure-volume loops in cardiac resynchronization therapy patients, Heart Rhythm 11 (3) (2014) 394–401.
[35] C. Pappone, Ž. Ćalović, G. Vicedomini, et al., Improving cardiac resynchronization therapy response with multipoint left ventricular pacing: twelve-month follow-up study, Heart Rhythm 12 (6) (2015) 1250–1258.
[36] L.F. Pavarino, S. Scacchi, S. Zampini, Newton–krylov-BDDC solvers for nonlinear cardiac mechanics, Comput. Methods Appl. Mech. Eng. 295 (2015) 562–580.
[37] M. Pennacchio, G. Savaré, P. Colli Franzone, Multiscale modeling for the bioelectric activity of the heart, SIAM J. Math. Anal. 37 (4) (2006) 1333–1370.
[38] D. Pittarello, V. Vida, G. Di Gregorio, et al., Comparison between pressure recording analytical method and fick method to measure cardiac output in pediatric cardiac surgery, Open Anesthesiol. J. 12 (1) (2018) 8–18.
[39] P. Ponikowski, A.A. Voors, S.D. Anker, et al., ESC guidelines for the diagnosis and treatment of acute and chronic heart failure, Eur. Heart J. 37 (27) (2016) 2129–2200, 2016.
[40] A. Quarteroni, A. Manzoni, C. Vergara, The cardiovascular system: mathematical modelling, numerical algorithms and clinical applications, Acta Numer. 26 (2017) 365–590.
[41] R. Ranjan, N. Chiamvimonvat, N.V. Thakor, et al., Mechanism of anode break stimulation in the heart, Biophys. J. 74 (4) (1998) 1850–1863.
[42] C.A. Rinaldi, C. Leclercq, W. Kranig, et al., Improvement in acute contractility and hemodynamics with multipoint pacing via a left ventricular quadripolar pacing lead, J. Intervent. Card Electrophysiol. 40 (1) (2014) 75–80.
[43] D.E. Roberts, L.T. Hersh, A.M. Scher, Influence of cardiac fiber orientation on wavefront voltage, conduction velocity, and tissue resistivity in the dog, Circ. Res. 44 (5) (1979) 701–712.
[44] S. Romagnoli, S. Bevilacqua, C. Lazzeri, et al., Most care: a minimally invasive system for hemodynamic monitoring powered by the pressure recording analytical method (pram), HSR Proc. Intensive Care Cardiovasc. Anesth. 1 (3) (2009) 20–27.
[45] S.M. Romano, M. Pistolesi, Assessment of cardiac output from systemic arterial pressure in humans, Crit. Care Med. 30 (8) (2002) 1834–1841.
[46] D. Romero, R. Sebastian, B.H. Bijnens, et al., Effects of the purkinje system and cardiac geometry on biventricular pacing: a model study, Ann. Biomed. Eng. 38 (4) (January 2010) 1388–1398.
[47] B.J. Roth, A mathematical model of make and break electrical stimulation of cardiac tissue by a unipolar anode or cathode, IEEE Trans. Biomed. Eng. 42 (12) (1995) 1174–1184.
[48] B.J. Roth, J. Chen, Mechanism of anode break excitation in the heart: the relative influence of membrane and electrotonic factors, J. Biol. Syst. 7 (4) (1999) 541–552.
[49] M. Sermesant, R. Chabiniok, P. Chinchapatnam, et al., Patient-specific electromechanical models of the heart for the prediction of pacing acute effects in CRT: a preliminary clinical validation, Med. Image Anal. 16 (1) (2012) 201–215.
[50] J.B. Tahri, T.F. Hansen, H.S. Storkås, et al., Interlead electrical delays and scar tissue: response to cardiac resynchronization therapy in patients with ischemic cardiomyopathy, Pacing Clin. Electrophysiol. 42 (5) (March 2019) 530–536.
[51] D. Tamborero, L. Mont, R. Alanis, et al., Anodal capture in cardiac resynchronization therapy implications for device programming, Pacing Clin. Electrophysiol. 29 (9) (2006) 940–945.
[52] K.H.W.J. ten Tusscher, A.V. Panfilov, Alternans and spiral breakup in a human ventricular tissue model, Am. J. Physiol. Heart Circ. Physiol. 291 (3) (2006) H1088–H1100.
[53] T.P. Usyk, A.D. McCulloch, Electromechanical model of cardiac resynchronization in the dilated failing heart with left bundle branch block, J. Electrocardiol. 36 (2003) 57–61.
[54] S.T. Wall, J.M. Guccione, M.B. Ratcliffe, et al., Electromechanical feedback with reduced cellular connectivity alters electrical activity in an infarct injured left ventricle: a finite element model study, Am. J. Physiol. Heart Circ. Physiol. 302 (1) (2012) H206–H214.
[55] J.P. Wikswo, S.F. Lin, R.A. Abbas, Virtual electrodes in cardiac tissue: a common mechanism for anodal and cathodal stimulation, Biophys. J. 69 (6) (1995) 2195–2210.
[56] F. Zanon, E. Baracca, G. Pastore, et al., Multipoint pacing by a left ventricular quadripolar lead improves the acute hemodynamic response to CRT compared with conventional biventricular pacing at any site, Heart Rhythm 12 (5) (2015) 975–981.